Cherenkov emission-based external radiotherapy dosimetry: I. Formalism and feasibility

Yana Zlateva[a)]
Medical Physics Unit, McGill University, Montreal, QC H4A 3J1, Canada

Bryan R. Muir
Metrology Research Centre, National Research Council Canada, Ottawa, ON K1A 0R6, Canada

Issam El Naqa
Department of Radiation Oncology, University of Michigan, Ann Arbor, MI 48103-4943, USA

Jan P. Seuntjens
Medical Physics Unit, McGill University, Montreal, QC H4A 3J1, Canada

(Received 17 April 2018; revised 6 January 2019; accepted for publication 7 January 2019; published 29 April 2019)

Purpose: Cherenkov emission (CE)-based external beam dosimetry is envisioned to involve the detection of CE directly in water with placement of a high-resolution detector out of the field, avoiding perturbations encountered with traditional dosimeters. In this work, we lay out the groundwork for its implementation in the clinic and motivate CE-based dosimeter design efforts. To that end, we examine a formalism for broad-beam in-water CE-based dosimetry of external radiotherapy beams, design and test a Monte Carlo (MC) simulation framework for the calculation of CE-to-dose conversion factors used by the formalism, and demonstrate the experimental feasibility of this method.
Methods: The formalism is conceptually analogous to ionization-based dosimetry and employs CE-to-dose conversion factors, $k_{\mathrm{C}}^{\theta \pm \delta\theta}$, including only and all CE generated within polar angles $\theta \pm \delta\theta$ on beam axis. The EGSnrc user code SPRRZnrc is modified to calculate $k_{\mathrm{C}}^{\theta \pm \delta\theta}$, as well as CE spectral and angular distributions. The modified code is tested with monoenergetic parallel electrons on a thin water slab. Detector configurations are examined for broad 6–22 MeV electron beams from a BEAMnrc TrueBeam model, with a focus on $\theta \pm \delta\theta = 90^\circ \pm 90^\circ$ (4π detection), $90^\circ \pm 5^\circ$, and $42^\circ \pm 5^\circ$ ($\theta = 42^\circ$ is the CE angle of relativistic electrons in water). We perform a relative experimental validation at 90° with electron beams, using a simple detector design with spherical optics and geometrical optics approximation of the sensitive volume, which spans the water tank. Due to transient charged particle equilibrium, broad photon beams are generally less sensitive to beam quality, depth, and angle.
Results: For 0.1–50 MeV electrons on a thin water slab, the code outputs CE photon spectral density per unit mass (calculated from dose and $k_{\mathrm{C}}^{\theta \pm \delta\theta}$) and angle in agreement with theory within ±0.03% and ±0.01°, respectively, corresponding to the output precision. The 42° configuration was found impractical due to detection considerations. Detection at $90^\circ \pm \delta\theta$ for small $\delta\theta$ exhibited beam quality dependence of the same order as well as strong superficial depth dependence. A 4π configuration ameliorates these effects. A more practical approach may employ a large numerical aperture. In comparing with literature, we find that these effects are less pronounced for broad photon beams in water, as expected. Measured relative $k_{\mathrm{C}}^{90^\circ \pm \delta\theta}$ at small $\delta\theta$ were within 1% of simulated factors (relative to their local average) for percent-depth CE (PDC) >50%. At other depths, deviations were in accordance with signal-to-noise, known detector limitations, and approximations. It was found that the CE spectrum is beam quality and depth invariant, while for electron beams the CE angular distribution is strongly dependent on beam quality and depth. However, the uncertainty of CE and PDC measurement at $90^\circ \pm \delta\theta$ detection for small $\delta\theta$ due to $\pm 0.1^\circ$ deviations around $\delta\theta$ was shown to be ≤1% and <0.1% ($k = 1$), respectively. The robustness to expected detector setup variations was found to result in ≤1% ($k = 1$) local uncertainty contribution for PDC >50%.
Conclusions: Based on our MC and experimental studies, we conclude that the CE-based method is promising for high-resolution, perturbation-free, three-dimensional dosimetry in water, with specific applications contingent on comprehensive detector development and characterization. *© 2019 American Association of Physicists in Medicine* [https://doi.org/10.1002/mp.13414]

Key words: Cerenkov, Cherenkov, dosimetry formalism, experimental validation, external radiotherapy beams, Monte Carlo

1. INTRODUCTION

Current routine radiotherapy dosimetry methods employ non-water-equivalent detectors, resulting in a necessary dose-to-water conversion as well as possibly significant field perturbation and volume averaging across the detection medium. In this work, we examine the feasibility of Cherenkov emission (CE)[1–3] dosimetry based on in-water CE detection with an out-of-field detector system with potential resolution of the order of micrometers.[4,5] Despite recent progress,[6,7] clinically implementable CE-based dosimetry system and protocol have not been established and data for converting CE to dose are not yet available. We motivate CE-based dosimetry detector and protocol development studies by considering a potential broad-beam[8] central-axis in-water CE-to-dose conversion formalism and modifying and experimentally evaluating EGSnrc[9] for the calculation of the broad-beam CE-to-dose conversion on beam axis in water, which is a useful starting point.

Quantitative studies of CE by external radiotherapy beams for the purpose of dosimetry have been published by Helo et al.[6] and Glaser et al.[7] Helo et al. investigate CE for use in quality assurance tests, such as range and field size verification of electron beams, via Monte Carlo (MC) and experiment. They find that CE imaging can be used to predict the practical range to within 3 mm for the 6, 9, and 12 MeV clinical electron beams studied and to measure the field width at 50% of the maximum dose. They conclude that CE can be used for quick routine quality assurance spot checks of electron beam range and field width constancy. Glaser et al.[7] carry out MC studies of CE by photon, electron, and proton beams in water. They state that in order for a CE-based dosimetry method to be viable, the CE-to-dose ratio must ideally be independent of position in the irradiated medium. They conclude that CE-based dosimetry is not feasible for clinical beams with some exceptions (e.g., intensity-modulated treatment plan verification). Here, we confirm that CE-to-dose ratios are position dependent and can be calculated via MC for clinical beams. The primary objective of this work is to incorporate and examine, from first principles, the broad-beam CE-to-dose conversion in a mathematical context as part of a formalism.

Our work is organized into two complementary papers. In this paper (Paper I), we (a) present a potential broad-beam central-axis CE-to-dose conversion formalism, (b) design and test the MC method for calculating conversion factors, and (c) validate our code through a relative experimental study with electron beams in water and with a simple detector design. The formalism applies to both photon and electron beams, while the calculation framework is validated experimentally with electron beams in water, for which we find that the relative conversion is more strongly dependent on depth, beam quality, and angle by comparison with the literature on broad photon beam CE-based dosimetry in water.[7,10,11] In the companion paper (Paper II),[12] which is motivated by the results of this paper (Paper I) and is focused entirely on electron beams, we calculate and examine the conversion for a clinically representative library of validated electron beam models, address electron beam quality specification, and evaluate a potential dosimetric uncertainty budget at a reference depth in water.

2. SETUP AND FORMALISM

The setup we envision for CE-based dosimetry on beam axis in water is shown in Fig. 1. The broad-beam CE-based formalism presented below applies to CE detection with narrow response on the beam axis, indicated by the square in Fig. 1. This requires optical design and characterization of a dedicated CE detection system, potentially including a customized phantom geometry and extension to two (2D) or three dimensions via focal spot scanning or a detector array. Out-of-focus removal and narrowing of the response at a distance from the optics is done in confocal microscopy as well as in optical section microscopy (without an excitation laser and by means of, e.g., nearest-neighbor deblurring).[5] Detector development is beyond the scope of this work and will require considerable resources and further investigation. The aim of this paper is to motivate this investigation by examining the broad-beam CE-to-dose conversion on beam axis in water, from first principles and with a simple detector.

The clinical endpoint (e.g., CE-based absolute vs relative dosimetry, large- vs small-field dosimetry, and MR-linac applications) is a related issue as it requires detector design and characterization. Absolute conversion of CE to dose may be feasible in a controlled phantom environment. No matter the outcome of a detector development study, it is of scientific interest to examine the absolute beam-axis CE-to-dose conversion for a broad-beam geometry in water.

To this end, we calculate the conversion via MC and we validate our code through a relative experimental study with a simple detector, built in-house with two plano-convex lenses + apertures feeding into a multimode optical fiber (Section 3.B). Therefore, the sensitive volume spans the entire

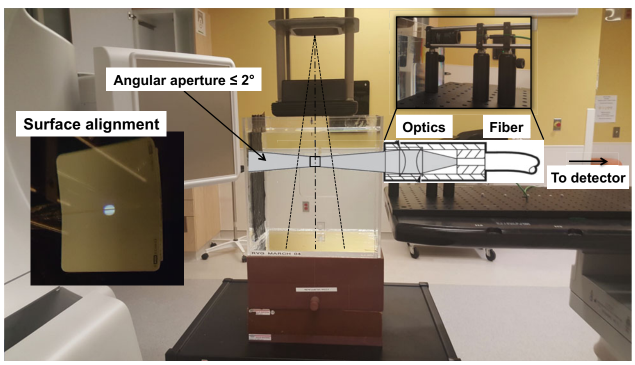

FIG. 1. Experimental setup for the detection of Cherenkov emission in water. Diagram is not to scale. Inset: Image of the light circle formed in the far field at the water surface by an LED source illuminating the detector end of the optical fiber (captured from outside the tank and below the surface). [Color figure can be viewed at wileyonlinelibrary.com]

water tank, as indicated by the gray double cone in the water in Fig. 1, and we compare MC-calculated to measured CE depth scans within this large sensitive volume, approximated via ray optics and assuming uniform response across it.

We now describe a potential broad-beam, central-axis CE-based dosimetry formalism. A sample schematic for this purpose is shown in Fig. 2. Under reference conditions for which the calibration and conversion apply, we have a broad beam[8] of quality Q depositing dose D in a small volume on beam axis and generating an anisotropic CE signal.[3] A portion of the CE angular distribution within the polar angle range $\theta \pm \delta\theta$, defined by the optics angular aperture (discussed below), is sampled and detected as a reading M. The equation we propose for relating M to D under reference conditions is the following:

$$D(Q) = MNk_{\mathrm{C}}^{\theta\pm\delta\theta}(Q), \tag{1}$$

where

$$M = M_{\mathrm{raw}}(SSD, x, y, z, FS)P_{\mathrm{T}}, \tag{2}$$

$$k_{\mathrm{C}}^{\theta\pm\delta\theta} = \frac{\int_{\Delta}^{E_{\max}} \Phi_E(E)L_\Delta(E)\mathrm{d}E + \Phi_E(\Delta)S_{\mathrm{col}}(\Delta)\Delta}{\int_{E_{\mathrm{thr}}}^{E_{\max}} \Phi_E^{\theta\pm\delta\theta}(E)S_{\mathrm{CE}}(E,\epsilon)\mathrm{d}E}, \tag{3}$$

$$S_{\mathrm{CE}}(E,\epsilon) = \frac{\alpha}{\hbar c}\left(1 - \frac{1}{n(\epsilon)^2\beta(E)^2}\right), \tag{4}$$

where the involved quantities are defined as:

- Q: beam quality specifier, which may or may not be the same as in current protocols[8,13] based on the associated uncertainty contributions.
- M: measured background-subtracted optical spectral density reading, M_{raw}, under the reference conditions of SSD, point of measurement, field size, FS, and temperature, T, for which the calibration and conversion apply. The temperature correction factor, P_{T}, stems from the temperature dependence of the refractive index, n,[14] and is discussed in greater detail in Paper II.[12]
- N: response calibration of the optical detector system, corresponding to the ratio of CE per unit mass generated at polar angles in the range $\theta \pm \delta\theta$ relative to the beam direction to detector reading. The angles are discussed below. The calibration would be obtained via a calibration lamp, traceable to a primary standards laboratory, and independent of ionizing radiation beam quality for optical systems with uniform response in the CE signal range, which may give CE-based dosimetry a distinct advantage over current methods.
- $k_{\mathrm{C}}^{\theta\pm\delta\theta}$: CE-to-dose conversion factor, including only and all CE at polar angles in the range $\theta \pm \delta\theta$ relative to the beam direction, which is determined by the detection optics angular aperture (AA, i.e., the acceptance half-angle). The AA is defined as the angular size, relative to the optical axis, of the optical aperture as seen from the focal point. Because CE is anisotropic[3] and optics have a limited AA, it is necessary to consider the portion of the CE angular distribution sampled by the optics. Only polar angles are considered, because the azimuthal component of the optics AA can be made 2π via azimuthal integration (e.g., rotation about the beam axis) or it can be included in the calibration, N, (together with the detector response) and would not vary in the azimuthal direction for symmetric beams. This also serves to improve the simulation statistics.
- Δ: Spencer–Attix cut-off energy.[15]
- E_{thr}: CE threshold energy (260 keV over the visible spectrum in water).[3,14]
- $E_{\max}$: maximum particle kinetic energy at the point of measurement.
- Φ_E: total (primary and secondary) charged particle fluence spectrum, differential in energy, at the point of measurement.

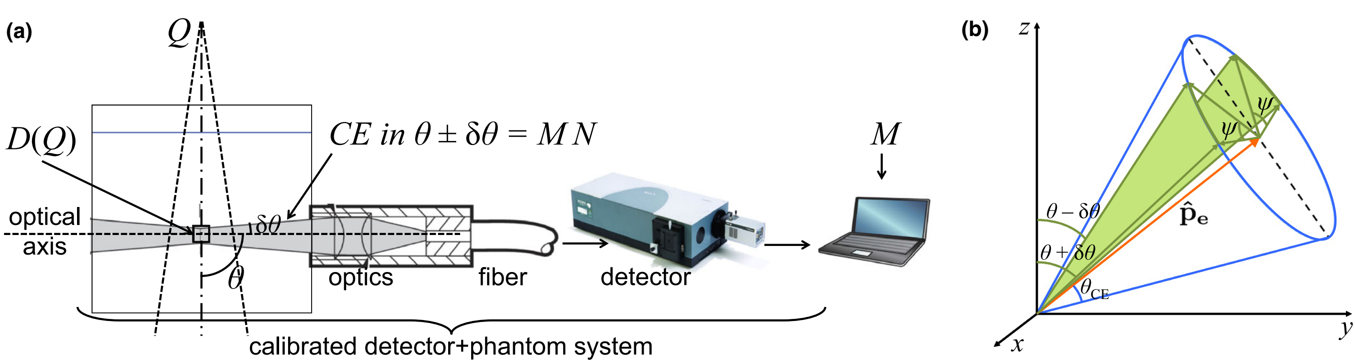

FIG. 2. (a) Sample Cherenkov emission (CE) detection setup for CE-based dosimetry of external radiotherapy beams, with variables defined in Eq. (1). Not to scale. (b) Sample geometry for scoring the fraction, $2\psi/2\pi$, of CE photons generated by electron of momentum unit vector $\hat{\mathbf{p}}_e$ (corresponding to CE angle θ_{CE}) that fall within $\theta \pm \delta\theta$. Note that the axes are rotated 180° about the x-axis in (a) to facilitate visualization. [Color figure can be viewed at wileyonlinelibrary.com]

$\Phi_E^{\theta\pm\delta\theta}$: total fluence spectrum, differential in energy, of charged particles with CE polar angles in the range $\theta \pm \delta\theta$ at the point of measurement.

L_Δ: charged particle restricted collision stopping power.

S_{CE}: CE power, expressed as the Frank–Tamm differential[2] and defined as the CE photon count differential in CE energy, ϵ, and path length of a charged particle of energy E corresponding to velocity β (in units of the speed of light in vacuum, c).

Integration over charged particle types is implicit in Eq. (3). Note that in contrast to ion chamber dosimetry, where the measurement medium is a gas,[8,16] pressure and humidity do not have any effect on M in CE-based dosimetry [see Eq. (2)].

Equation (1) applies to both photon and electron beams. The conversion from M to CE at $\theta \pm \delta\theta$, including the system response and azimuthal AA, is contained in the system calibration N. The conversion from CE at $\theta \pm \delta\theta$ to D is contained in the CE-to-dose conversion factor $k_C^{\theta\pm\delta\theta}$. The $k_C^{\theta\pm\delta\theta}$ factor in Eq. (3) is the ratio of dose according to Spencer–Attix theory[15] to CE per unit mass within $\theta \pm \delta\theta$, under reference conditions. Note that these should be mass stopping and CE powers, but the density of the cavity material is the same. In addition, the CE integral has no track-end term as there is no CE below the threshold E_{thr}.

The unrestricted collision stopping power[17] and CE power[2] [Eq. (4)] are plotted as a function of electron kinetic energy in Fig. 3 for energies in the range 0.1–10 MeV in water (n = 1.34).[14] It is clear from this figure and from Eq. (3) that the $k_C^{\theta\pm\delta\theta}$ factor is beam quality and depth dependent, because the stopping power and CE power are different functions of charged particle energy integrated from different low-energy thresholds in the charged particle fluence spectrum.

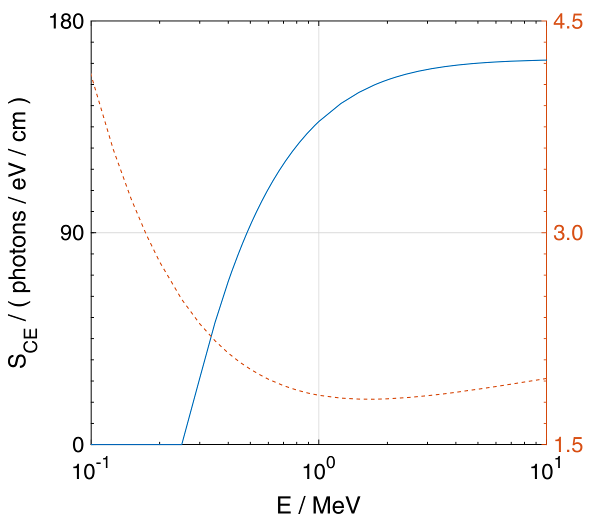

FIG. 3. Cherenkov emission (CE) power [Eq. (4) with n = 1.34] and unrestricted collision stopping power (right y-axis, dashed line) as functions of electron kinetic energy in the range 0.1–10 MeV in water.[2,14,17] [Color figure can be viewed at wileyonlinelibrary.com]

3. MATERIALS AND METHODS

3.A. Monte Carlo calculation of conversion factors

3.A.1 BEAMnrc model and parameters

Beams are simulated with the BEAMnrc code[18,19] of the particle transport simulation package EGSnrc.[9,20] The experimental validation study focuses on electron beams, which tests the limits of the code performance due to higher overall sensitivity to beam quality, depth, and angle than for photon beams.[7,10,11] Our clinical machine is a Varian TrueBeam, whose BEAMnrc model data and parameters were provided by the vendor (Varian Medical Systems, Inc., Palo Alto, CA).[21] Eight electron beams were simulated with nominal energies of 6–20 and 22 MeV at 10 × 10-cm^2 and 20 × 20-cm^2 field size, respectively, and 100-cm SSD.[8]

3.A.2 SPRRZnrc modifications and parameters

BEAMnrc-generated incident phase space data were input into a modified version[22] of the SPRRZnrc code,[23] which calculates Spencer–Attix mass restricted collision stopping-power ratios[15] by summing contributions from charged particle steps on-the-fly. SPRRZnrc was adapted to calculate $k_C^{\theta\pm\delta\theta}$ factors according to Eq. (3) by: (a) using a homogeneous water phantom; (b) modifying the code to score CE power within $\theta \pm \delta\theta$ in water instead of stopping power in a different medium;[2] and (c) setting the Spencer–Attix cut-off Δ for scoring the dose to 10 keV (electron CSDA range = 3 μm in water)[17] and the CE threshold for scoring CE to 257 keV for refractive index of 1.34,[2] which corresponds to a minimum (at 500 nm) in optical absorption by water at room temperature.[14,24]

Detection of CE depends on the overlap of the detection geometry with the CE cone, which varies with charged particle energy and direction. A sample geometry for scoring CE by an electron with momentum unit vector $\hat{\mathbf{p}}_\mathbf{e} = [\mathbf{u}, \mathbf{v}, \mathbf{w}]$, corresponding to CE cone angle $\cos\theta_{CE} = (n\beta)^{-1}$,[3] is shown in Fig. 2(b). The CE photons generated within the polar angle range $\theta \pm \delta\theta$ are indicated as the solid green (online version only) areas of the cone surface. The fractional CE photon yield within $\theta \pm \delta\theta$ is equivalent to the fractional arc length $2\psi/2\pi$. The latter is related to charged particle energy and direction for a given step through the CE angle θ_{CE}[3] and the particle z direction cosine $\| \mathbf{w} \|$, respectively. The $2\psi/2\pi$ term is included in $\Phi_E^{\theta\pm\delta\theta}$ in Eq. (3) and used to weight the CE power S_{CE} in scoring the $k_C^{\theta\pm\delta\theta}$ factor in the code.

The code outputs dose per incident fluence, as well as $k_C^{\theta\pm\delta\theta}$ as energy deposited per CE photon spectral density at n = 1.34 in units of MeV · eV · photon^{-1}. From this, we calculate CE photon spectral density per mass per incident fluence (under the same conditions). A thin-slab test was performed to ensure the modified code behaves correctly in accordance with the CE theory.[3] This entailed simulating monoenergetic parallel electron beams of 0.1–50 MeV energies and 1-cm radius incident on a water slab of 10-cm radius and 1-pm width along the beam axis. The width was chosen to ensure that electrons traverse the thin slab without energy loss and in a straight line, so that their energy, path length, and direction are exactly known. This allows to calculate the theoretical CE photon spectral density per unit mass as the denominator of Eq. (3) [using Eq. (4) and normalizing by mass density] and the theoretical CE angle, $\cos\theta_{\mathrm{CE}} = (n\beta)^{-1}$.[3,14]

The considered $\theta \pm \delta\theta$ for the clinical electron beam simulation are $90° \pm 90°$ (4π detection), $90° \pm 5°$, and $42° \pm 5°$. The 42° angle is the CE angle of relativistic electrons in water,[3,14] which constitute the bulk of the fluence spectrum, scatter the least, and have the highest CE power.[2] Therefore, the 42° configuration provides the highest signal within a constrained angular aperture. However, 42° relative to the surface tangent is also the angle of total internal reflection at a water–air interface[14] and, therefore, the detector must be placed in the water with conventional phantom geometries (e.g., cubic/cylindrical). Alternatively, reflection losses can be mitigated with a nonconventional phantom geometry. On the other hand, detection at 90° is simplest in terms of setup, allowing detector positioning in air with the use of a simple phantom as it entails minimal reflectance loss at a phantom exit surface that is parallel to the beam (e.g., cubic/cylindrical phantom). Lastly, the 4π configuration may require 4π detection or complete conversion to an isotropic signal with the use of a fluorophore as has been suggested in previous work.[25] This, however, would introduce additional uncertainty contributions of the fluorophore quantum yield, potential deviation from isotropic fluorescence, and scintillation.[26] The CE scoring polar angle range $\theta \pm \delta\theta$ was added as an input to the modified SPRRZnrc code, with a default value of $90° \pm 90°$ (i.e., 4π detection).

Unless otherwise specified, the default EGSnrc transport parameters were used.[20] For the MC validation study, the length of the scoring bins along the depth direction was 0.2 cm. Typically of the order of 10^7–10^8 histories were simulated at incidence (of the order of 1–10 CPU hours, Intel Xeon E5-2687W) to ensure dose uncertainty at $d_{\max}$ within 0.3%. To initiate future efforts toward detector development via optical design of a CE-based dosimeter, we also extended the code to score CE spectral and angular distributions.[3]

3.B. Experimental validation

Experiments were carried out on a Varian TrueBeam with nominal electron beam energies of 6, 12, and 20 MeV, at 90° detection, and with the setup shown in Fig. 1. The beam was centered on a 30-cm cubic polycarbonate tank with 6-mm walls filled with deionized water. We use a simple detector prototype, built in-house from a minimum number of components, including two spherical lenses and a multimode optical fiber, with a detection volume that is focused on beam axis and spans the water tank as indicated by the gray double cone in the water in Fig. 1. This serves to also validate the MC calculations in the penumbra region, which is included in the sensitive volume, and for angular variations about the 90° detection angle. In addition, by focusing the optics to the central beam axis, we take account of the lateral positioning uncertainty contribution of focusing on beam axis, as opposed to focusing away from beam axis or using an unfocused setup (e.g., a fiber without lenses).

The detector system was composed of a diffraction grating spectrometer (Shamrock 193i, SR2-GRT-0300-0500 grating, Andor Technology Ltd, Belfast, UK), with a pair of plano-convex spherical lenses (N-BK7, AR Coating: 350–700 nm, Thorlabs, Inc., Newton, NJ, USA) focusing into a 15-m, high-OH, NA = 0.22, MFD = 0.1 mm optical fiber input (93% transmittance at 500 nm, source: Thorlabs, Inc., Newton, NJ, USA), and a cooled to −80°C back-illuminated CCD (Newton EMCCD, 1600 × 200, 16 μm pixels, Andor Technology Ltd., Belfast, UK). To reduce readout noise, the full CCD chip was used and binned in the vertical direction (200 pixels) and, because CE is a broadband signal, the (horizontal) wavelength resolution was binned to 2 nm during readout. For the depth scan studies, spectra were binned from 400 to 600 nm during postprocessing. A long fiber was used to allow positioning of the spectrometer and CCD outside the treatment room to avoid their irradiation. To minimize spherical aberration, a pair of plano-convex lenses were used, oriented as in Fig. 2, and the AA was limited with a pair of apertures adjacent and on the outside of the lens pair.[27] The focal point cross-section (perpendicular to the optical axis) in water was 0.5 mm with the largest AA (±2°). The optics were mounted on a cage system attached to a laser table, which was positioned on the couch for remote depth scanning and aligned with the treatment room lasers.

Optical alignment was achieved with a broadband LED source passed through the fiber (disconnected from the spectrometer) and optics in the reverse direction of CE detection. The fiber was positioned at the focal point of the focusing lens (i.e., the right lens in Fig. 2, which focuses CE into the fiber) by checking collimation of the light source with that lens alone in air. The focal point in water together with the radiation beam were centered on the water phantom to ensure a symmetric measurement volume (and thus minimize its depth extent) by verifying that the AA diameters at the near and far tank walls were within 0.5 mm of each other. Depth positioning was achieved by aligning the light source image, shown in Fig. 1, at the water surface in the far field, in a manner analogous to ionization-based dosimetry.[28]

Experiments were done with optical blackout material covering the entire setup to eliminate stray light, as well as on the far wall of the tank, as seen in Fig. 1, to eliminate reflections. The background readings in the fiber and in the tank wall near the detector were acquired with the inside of the wall covered with blackout material. Depth CE was scanned remotely with the couch controls. Depth dose was scanned with an IBA CC13 ionization chamber. The purpose of the experimental validation is to make a first-order estimate of the uncertainty on the CE-to-dose conversion based on the difference between MC and experiment. The results reported here are relative and could be improved and extended by use of diffraction-limited optics and absolute irradiance calibration of the detector system.

4. RESULTS

4.A. Thin slab test of the Monte Carlo CE calculation framework

It was verified for monoenergetic parallel electrons in the 0.1–50 MeV energy range that the simulated CE photon spectral density per unit mass (calculated from dose and $k_C^{\theta\pm\delta\theta}$) and the simulated CE angle in a 1-pm thin slab of water are in agreement with theory[3,14] to ±0.03% and ±0.01°, respectively, within the simulation precision of 1×10^{-4} MeV/(photon/eV). The relative difference between the theoretically calculated and simulated CE spectral density scored within ±0.01° of the theoretically calculated CE polar angle is plotted in Fig. 4 as a function of incident electron energy. It was also verified that the simulated CE spectral density at other angles is zero within the simulation precision.

4.B. Calculated $k_C^{\theta\pm\delta\theta}$ factors for electron beams from our clinical machine and detection angle optimization

The experimental validation with electron beams in Section 4.C involves a comparison of calculated and measured CE depth scans within the large double-cone sensitive volume indicated in gray in Fig. 1 (Section 3.B). As will become evident below in Section 4.D.2, the shape of the angular distribution is minimally affected by lateral integration of the sensitive volume. Therefore, since we are ultimately interested in the central-axis CE and k_C distributions, we take a closer look at them here and based on this we optimize the detection configuration for the experimental validation study that follows.

In Figs. 5 and 6, we show representative simulation results of the electron beam percent-depth dose (PDD), percent-depth CE (PDC) generated in all directions (4π) and at polar angles of 90° ± 5° and 42° ± 5° relative to the beam axis, as well as the corresponding PDD-to-PDC ratios. The latter are equivalent to CE-to-dose conversion factors, $k_C^{\theta\pm\delta\theta}$, for $\theta \pm \delta\theta \in \{90^\circ \pm 90^\circ(4\pi),\ 90^\circ \pm 5^\circ,\ 42^\circ \pm 5^\circ\}$, normalized by the ratio of dose to CE maximum, which is provided in the legend.

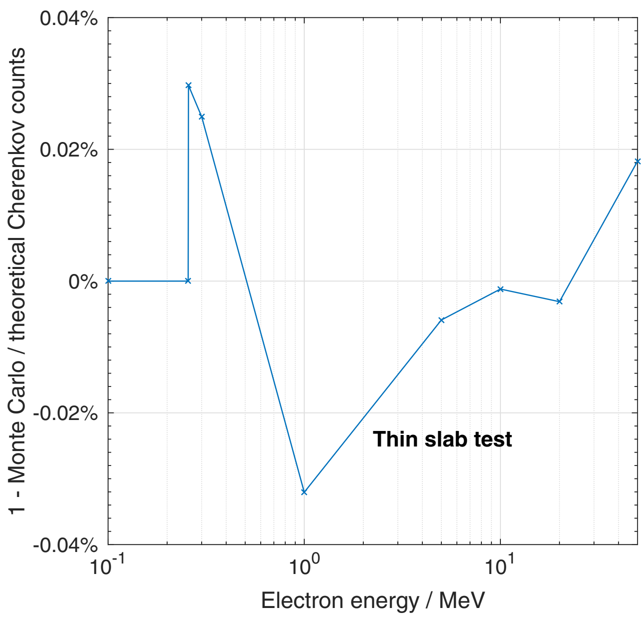

Fig. 4. Relative difference between theoretical and Monte Carlo-calculated Cherenkov emission (CE) photon spectral density generated at the theoretically calculated CE angle[3,14] ±0.01° in a thin water slab in terms of incident electron energy. [Color figure can be viewed at wileyonlinelibrary.com]

4.C. Agreement of calculated and experimental relative $k_C^{90^\circ\pm2^\circ}$ factors

In Figs. 7 and 8, we show representative experimental and corresponding simulation results with two electron beam qualities of the PDD, PDC at 90° to the beam with 2° AA, as well as the corresponding PDD-to-PDC ratios, which are essentially normalized CE-to-dose conversion factors k_C. The locally normalized difference between simulated and experimental relative k_C factors (i.e., PDD/PDC ratios), or equivalently between calculated PDD (as the product of the experimental PDC and the simulated relative k_C) and experimental PDD, is within 1% for PDC values higher than 50%. At shallow and large depths, the discrepancies are attributable to optical aberrations as well as reflections at the water–air interface.[14] This is discussed further in Section 5.

4.D. Detection considerations at $\theta = 90^\circ$

4.D.1 CE spectrum

In Fig. 9, we show simulated CE spectra in water and measured spectra at 90° to the beam for a range of electron beam qualities and depths, together with the Frank–Tamm equation for the CE spectrum of relativistic electrons ($\beta = 1$) in water.[2,14] The difference between the measured and simulated spectra arises mainly from the detector system spectral sensitivity. As we perform a relative experimental validation in order to motivate detector development, the depth invariance of the CE spectrum observed in Fig. 9 indicates that the spectral sensitivity is not relevant in the current context.

4.D.2 CE angular distribution

Simulated, broad electron beam, central-axis CE angular distributions at $n = 1.34$ in water[2,3,14] for a range of beam qualities and depths, normalized to their respective maxima, are shown in Figs. 10(a) and 10(b), normalized to solid angle and polar angle range $\delta\theta$, respectively. Normalization constants are also provided in terms of CE photons per unit CE

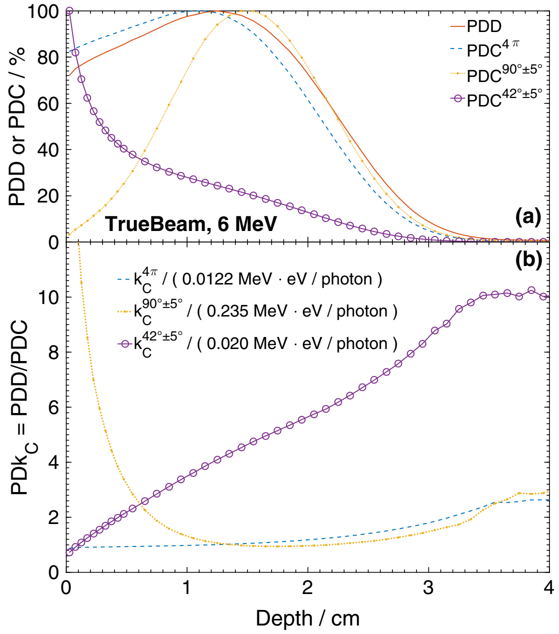

FIG. 5. Simulated (a) percent-depth dose, PDD, percent-depth Cherenkov emission, $PDC^{\theta\pm\delta\theta}$, and (b) normalized Cherenkov-to-dose conversion factors, $k_C^{\theta\pm\delta\theta}$, in water, at polar angles $\theta \pm \delta\theta$ of 90° ± 90° (4π), 90° ± 5°, and 42° ± 5° relative to the beam, for a TrueBeam 6 MeV electron beam. [Color figure can be viewed at wileyonlinelibrary.com]

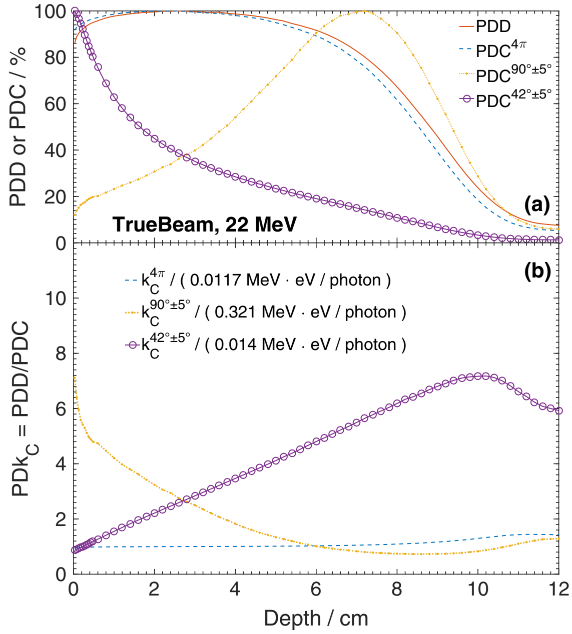

FIG. 6. Same as Fig. 5 but for TrueBeam 22 MeV electrons. [Color figure can be viewed at wileyonlinelibrary.com]

energy bandwidth, solid angle or $\delta\theta$, mass, and incident fluence to allow the reader to estimate the optical power (typically in the pW-nW range) for a specific application. The length of the scoring voxels was 2 mm in the depth direction. Please note that these values are provisional, contingent on absolute experimental validation and optimization of the code. For comparison with a 6-MV photon beam study,[10] in Fig. 10(c) the distributions are laterally averaged over a 100-cm radius water volume.

4.D.3 *Angular aperture*

Figure 11 shows simulation results at 90° detection with varying $\delta\theta$ for a 12 MeV beam as representative of both high and low energies. For illustrative purposes, the PDC is shown for ±4° variations in $\delta\theta$ about $\theta \pm \delta\theta = 90° \pm 5°$. However, $k_C^{\theta\pm\delta\theta}$ is nonlinear with $\delta\theta$. Therefore, to examine the dependence on small $\delta\theta$ variations, simulations were performed for ±0.1° variations about $\theta \pm \delta\theta = 90° \pm 5°$. The locally normalized difference was found to be within ±2.2% at all depths and beam energies.

Figure 12 is the experimental equivalent of Fig. 11 with AA of 2° (10-mm maximum aperture diameter at the tank wall) and 1° (5-mm maximum diameter). The 2° AA is the largest achievable with our setup and optics. The locally normalized % difference in this case is calculated from the absolute background-subtracted and mass-normalized optical readings (counts/s per ray optics-approximated sensitive volume mass) at 1° and 2° AA and therefore corresponds to ±0.5° variation about the average AA (1.5°).

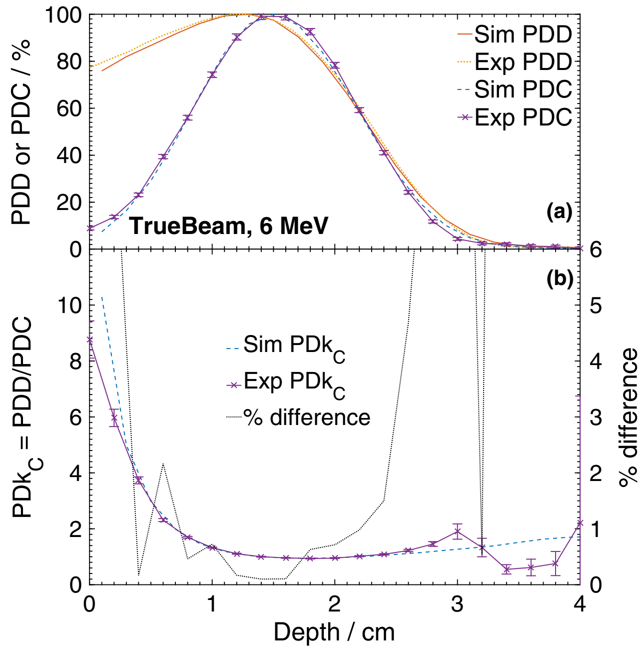

FIG. 7. (a) Simulated (Sim) and experimental (Exp) percent-depth dose, PDD, percent-depth Cherenkov emission, PDC, at 90° to the beam with ±2° angular aperture, and (b) corresponding PDD-to-PDC ratios, representing normalized Cherenkov-to-dose conversion factors, k_C, and their locally normalized % difference, in water for a TrueBeam 6 MeV electron beam, using the setup of Fig. 1. The error bars define an interval estimated to have 95% level of confidence, based on the t-distribution for 4 degrees of freedom (four acquisitions) and calculated solely from the experimental standard deviation of the mean background-subtracted optical reading at each depth. [Color figure can be viewed at wileyonlinelibrary.com]

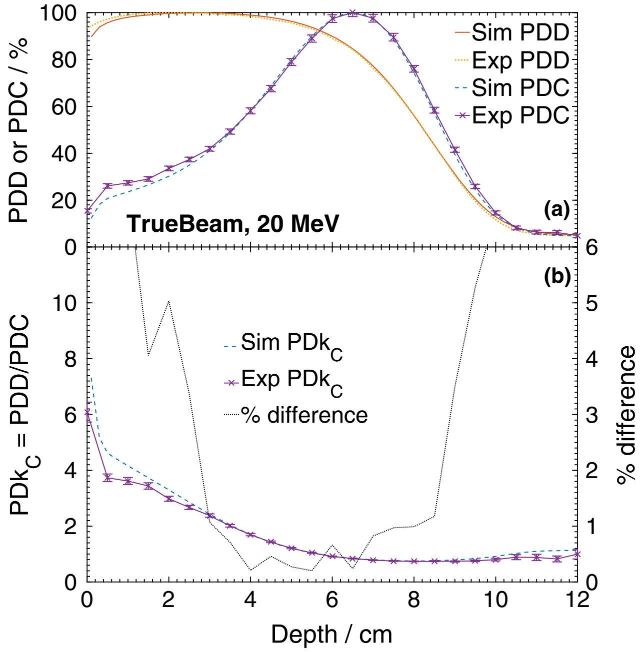

FIG. 8. Same as Fig. 7 but for TrueBeam 20 MeV electrons. [Color figure can be viewed at wileyonlinelibrary.com]

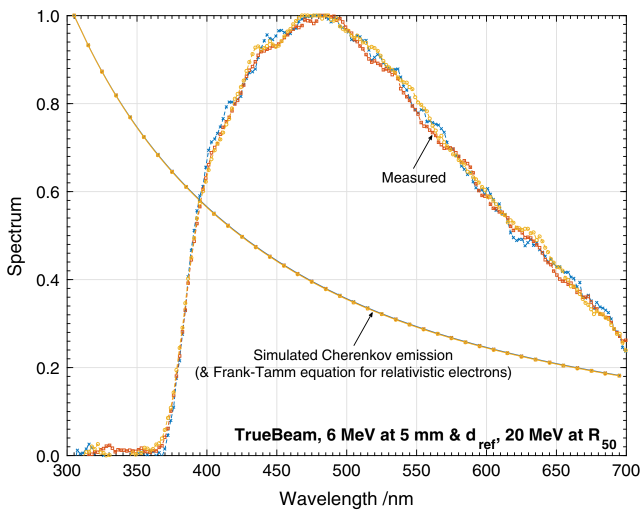

FIG. 9. Simulated CE and measured spectra at 90° to the beam of TrueBeam 6- and 20-MeV electron beams at various depths in water. The Frank–Tamm equation for relativistic electrons ($\beta = 1$) is also shown.[2,3] [Color figure can be viewed at wileyonlinelibrary.com]

4.D.4 Robustness

The uncertainty contribution stemming from the robustness of the measurement system, calculated from two measurement sessions separated by 7 days and involving reassembly, refocusing, and re-collimation of the detector head, changes in lens material, and ± 1 cm changes in lens focal length and position, was found to be up to 1% ($k = 1$) at PDC values higher than 50%. The results of this study at 90° detection with 2° and 0° AA are shown in Fig. 13.

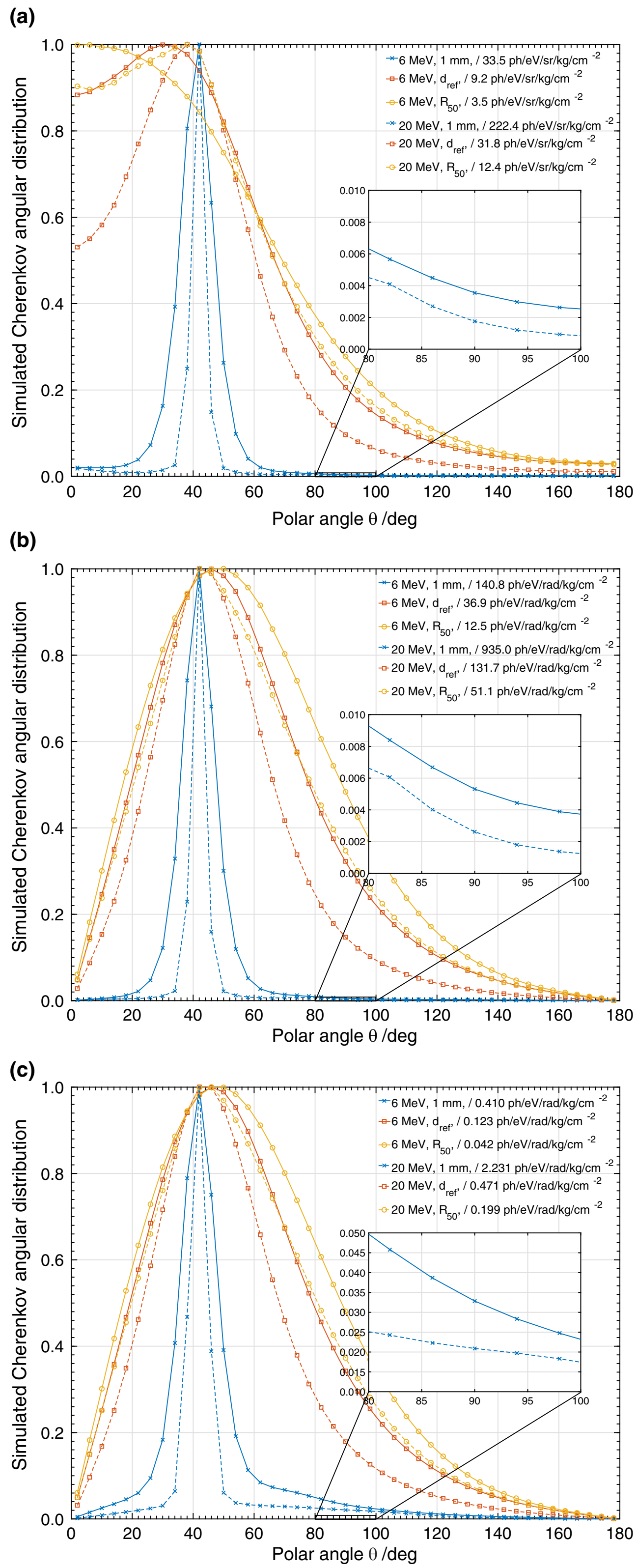

FIG. 10. (a) Simulated broad-beam, central-axis CE angular distributions of TrueBeam 6- and 20-MeV electron beams at n = 1.34 in water[2,3,14] at various depths. Normalization constants are shown in terms of CE photons per unit CE energy bandwidth, solid angle, mass, and incident fluence. (b) The CE angular distributions of (a) per unit polar angle instead of solid angle (i.e., azimuthally integrated). (c) The CE angular distributions of (b), but integrated over 100-cm water radius. [Color figure can be viewed at wileyonline library.com]

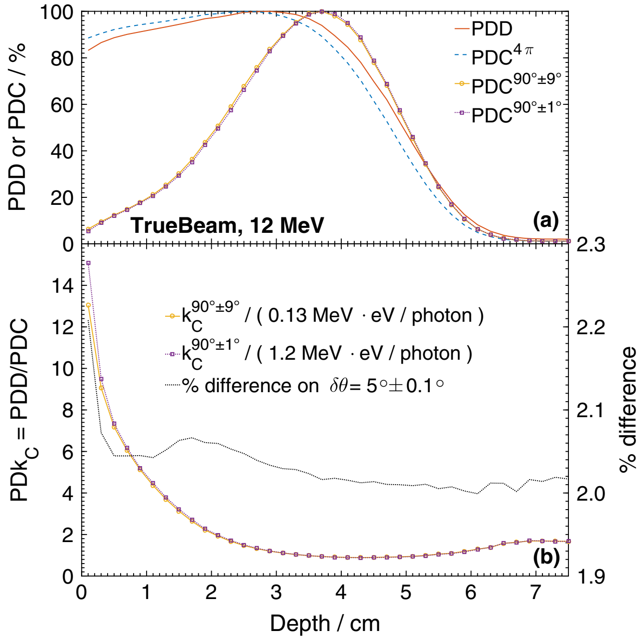

FIG. 11. Simulated (a) percent-depth dose, PDD, percent-depth Cherenkov emission (CE), $\mathrm{PDC}^{\theta\pm\delta\theta}$, at polar angles $\theta \pm \delta\theta$ of $90^\circ \pm 90^\circ$ (4π), $90^\circ \pm 9^\circ$, and $90^\circ \pm 1^\circ$ relative to the beam, and (b) corresponding normalized CE-to-dose conversion factors, $k_C^{\theta\pm\delta\theta}$, and locally normalized difference on absolute CE values corresponding to $\delta\theta$ variations of $\pm 0.1^\circ$ about 5°, in water for a TrueBeam 12-MeV electron beam. [Color figure can be viewed at wileyonlinelibrary.com]

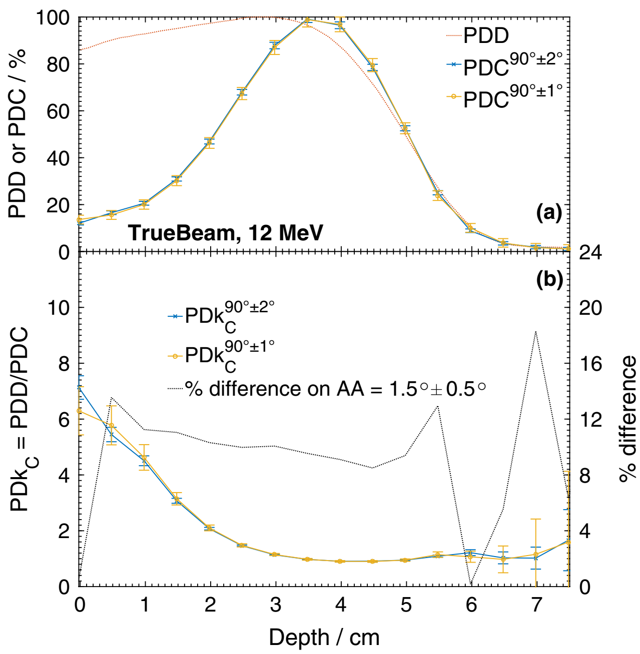

FIG. 12. Experimental equivalent of Fig. 11 but for optical angular aperture (AA) of 2° and 1° and corresponding locally normalized % difference on the absolute background-subtracted and mass-normalized optical readings (counts/s per ray optics-approximated sensitive volume mass). The error bars are computed as in Fig. 7. [Color figure can be viewed at wileyonlinelibrary.com]

The repeat measurement at 2° involved a switch from a 2-cm focal length (f/2) fused silica to a 5-cm focal length (f/2) N-BK7 focusing lens (right lens in Fig. 1), as well as

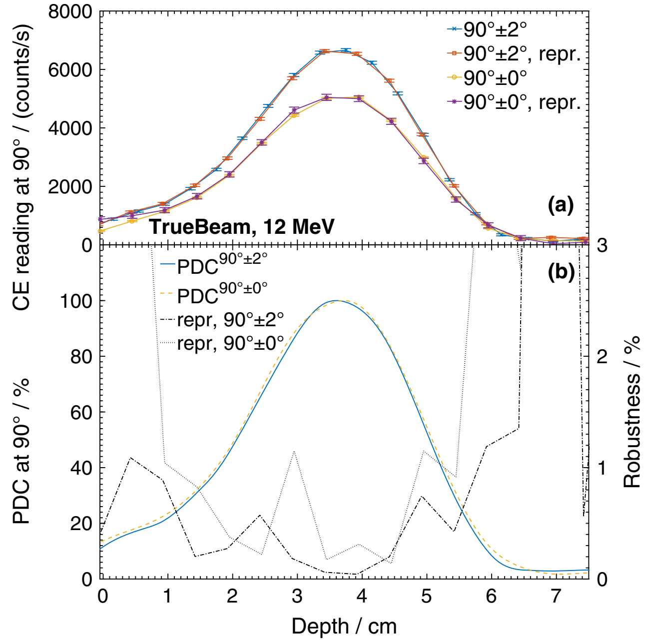

FIG. 13. (a) Experimental Cherenkov emission (CE) reading at 90° to the beam from repeat measurements at 2° and 0° angular aperture with optics reassembly, refocusing, and slight change of setup (namely, focusing lens shape for 2° and collimation for both 2° and 0°). The reproduced 0° curve (repr, $90^\circ \pm 0^\circ$) is volume-ratio normalized to account for aperture differences between the two experiments. (b) Corresponding averaged percent-depth CE, PDC, at 90° to the beam (error bars are not computed as they have no relevance to the discussion) and robustness, represented as relative standard uncertainty ($k = 1$). These results are for CE measurements in water from a TrueBeam 12-MeV electron beam, using the setup of Fig. 1. The error bars are computed as in Fig. 7. [Color figure can be viewed at wileyonlinelibrary.com]

insertion of an aperture between the fiber and the focusing lens to limit the AA. The 0° measurement in Fig. 13 involved the use of only a focusing lens. The repeat measurement at 0° involved decreasing the aperture diameter from 12 to 6 mm and normalizing by the corresponding volume ratio.

4.D.5 Background signal

There was no change in the CE background acquired by blacking out only the input optics instead of the inside face of the water tank wall near the detector, as described in Section 3.B, indicating that there is no CE contribution from the near wall. The CE background varied little in the z direction, which is characteristic of photon scatter, and it generally constituted up to 10% of the maximum raw signal with all energies depending on the aperture size and for couch shifts of the order of ± 1 cm. Variations in position and focal distance of the optics of 1 cm at constant couch position had no effect on the CE background, indicating that the background is mainly due to couch scatter. Contributions from the far-field wall of the water tank were estimated from measurements with and without blackout of the far wall and found to be up to ~5% of the local background-subtracted signal with all beam energies and characteristic of the electron PDC at 90°. This indicates that they are due to reflections of the in-field

CE and not CE from the wall itself. To eliminate this effect, all measurements were done with blackout of the far wall as explained in Section 3.B. Finally, increasing the radius of curvature of the curved side by 1 cm, or equivalently the focal distance by 2.5 cm, of the collimating lens (i.e., the left lens in Fig. 1) at constant (ray optics approximated) sensitive volume increased the signal by up to 2% of the maximum, which indicates that optical aberrations result in contributions from points outside the sensitive volume.

5. DISCUSSION

With recent progress[6,7,29,30] and increasing interest in the field for more than five years,[10] CE-based dosimetry is on its way to the clinic. However, a clinically implementable CE-based dosimetry protocol has not been established. Accurate CE-to-dose conversion factors have not yet been made available. Furthermore, a high-resolution CE-based dosimeter of demonstrated sufficient accuracy has yet to be designed. In this work, we provide necessary means to move the field further forward. In comparison with ionization-based dosimetry,[8,13] the sensitive volume in CE-based dosimetry is water and resolutions of the order of micrometers may potentially be achievable, contingent on a detector development study.[5,4,27] The absolute vs relative CE-based dosimetry endpoint is a matter of further investigation and also requires detector development. Here, we motivate this by considering, from first principles, a potential broad-beam central-axis CE-based dosimetry formalism applicable to both photon and electron beams, developing an EGSnrc[9] simulation framework for the calculation of the CE-to-dose conversion, and performing a relative experimental validation and feasibility study in water using a simple detector and with electron beams for which the relative conversion is more sensitive to depth, beam quality, and angle than for photon beams.[7,10,11] Although CE-based dosimetry might ultimately provide solutions to the challenges faced by ionization chambers in a different clinical situation (e.g., small fields and MR-linacs), we begin the investigation with a look into the broad-beam CE-to-dose conversion on beam axis in water.

Because CE is anisotropic,[3] we first investigate potential detection configurations for the experimental validation study with electron beams. In Figs. 5 and 6, we see that the electron beam central-axis PDC generated in 4π is upstream of the PDD. This is a consequence of the CE threshold energy[2] and is in agreement with Glaser et al.[7] and Helo et al.[6], where the Geant4-calculated[31] PDC generated in 4π was compared with the PDD of 6 and 9 MeV electron beams. A quantitative justification is provided in the companion Paper II, which is focused solely on electrons beams.[12] As a result, the CE-to-dose conversion is beam quality and depth dependent. The implications of this on CE-based electron beam dosimetry are also discussed in Paper II.

In contrast to the central-axis PDC generated in 4π, the PDC at polar angles of $\theta \pm \delta\theta$ for small $\delta\theta$ depends not only on the charged particle fluence but also on the scattering state of the beam due to the anisotropy of CE.[3] Therefore, as can be seen for electron beams in Figs. 5 and 6, the PDC at $90^\circ \pm 5^\circ$ to the beam exhibits a steeper build-up, in agreement with Helo et al.[6] for 6–12 MeV electrons, and is peaked at a larger depth than the 4π PDC, while the PDC at the 42° CE angle of relativistic electrons[3,14] is peaked at $z = 0$ cm and decreases drastically away from the surface as electrons lose energy and become less forward directed. Therefore, although it provides a strong signal within a constrained angular aperture,[2] the 42° configuration is impractical for dosimetric purposes as it not only requires in-water detector placement, or conversely a nonconventional phantom geometry, to correct for total internal reflection at the phantom wall,[14] but also normalization at $z = 0$ cm, which makes the measurement dependent on the size of the scoring volume. This in turn leads to a high uncertainty in the PDC-derived electron beam quality specifier (e.g., R_{50}[8] derived from the depth of 50% CE, discussed in Paper II).[12] Furthermore, at 42° we expect a high contribution from both depth and beam quality uncertainties due to the strong variation of $k_C^{42^\circ \pm \delta\theta}$ with depth and beam quality for small $\delta\theta$.

The 90° configuration, on the other hand, appears to be the most practicable of the three because it allows in-air detector positioning with minimal reflectance losses with conventional phantoms. However, although $90^\circ \pm \delta\theta$ for small $\delta\theta$ is less susceptible to depth positioning uncertainties for CE-based dosimetry performed at a reference depth near $d_{\max}$, it exhibits beam quality dependence of the same order as 42° and it is very depth-sensitive near the surface. With a 4π configuration, the beam quality and depth dependence is greatly reduced; however, a 4π detection geometry is required. This could potentially be achieved in water via tomographic reconstruction or with a small integrating sphere positioned on beam axis. The latter will, however, diminish the value of CE-based dosimetry as a perturbation-free technique. A more practical approach may employ an objective with a large numerical aperture and definition of the sensitive volume by means of a de-blurring technique, such as nearest neighbor.[5] Larger numerical apertures are considered in Paper II.[12] For broad photon beams in water, these effects are less pronounced[7,10,11] due to the existence of transient charged particle equilibrium (i.e., less variation of the charged particle fluence spectrum and angular distribution with depth). The experimental validation and feasibility here is performed with electron beams in water at 90° with AA of up to 2°.

As mentioned in Section 2, the CE-based formalism involves CE detection with narrow response centered on the beam axis.[4] In our experiments, the response spans the water tank. We assume it to be uniform across the entire ray optics-approximated acceptance volume in water (the solid gray double cone in the water tank in Fig. 1) and compare with MC depth scans of CE scored within this large volume. In Section 4.C, the dosimetric uncertainty contribution of the electron beam CE-to-dose conversion due to the difference between MC-calculated and experimental PDD-to-PDC ratios is estimated at 1% to first order at depths where the PDC is >50%. This excludes the contribution from absolute calibration of the CE-based dosimeter, which is a matter of further investigation. This is an improvement from Helo et al.[6], where a ruler was used for depth positioning and camera magnification was shown to have a significant effect. At shallow and large depths, the discrepancies observed between the measured and MC-calculated PDD-to-PDC ratios are attributable to optical aberrations and reflections at the water surface where the angle of total internal reflection is 48° with respect to the surface normal.[14] Because the point of interest is on the optical axis (see Fig. 2), the major aberrations at play are chromatic and spherical.[4] Off-axis aberrations likely also play a minor role, because a broad radiation beam (see Section 3) results in a spatially broad CE signal (an extended light source). Due to spherical aberration, marginal rays that are focused into the optical fiber originate from points on the optical axis closer to the optics than the point of best focus, while paraxial rays originate from points further away.[4] Therefore, because the point of best focus was centered on the radiation beam central axis, as explained in Section 3, spherical aberration increases the contribution of points lateral to the beam axis. At these lateral positions, the PDC at 90° is larger in the build-up and photon tail, which was also observed to be the case in our simulations.

The excellent agreement with the analytical Frank–Tamm spectrum[2] as well as the lack of variation with beam quality and depth observed in both simulation and experiment in Fig. 9 serve as further validation of our EGSnrc CE calculation framework.[9,20,23] The CE spectrum of high-energy electron beams is independent of the electron fluence spectrum since the electron energy dependence stems from the $1/\beta^2$ term [see Eq. (4)], which is slowly varying at relativistic energies.[2] The dose-CE relationship is therefore largely determined by the total fluence. This finding will facilitate detector design by relaxing the detector spectral response requirements. Furthermore, because the results of the experimental validation study of Section 4.C are relative and because the CE spectrum is depth-invariant, the system quantum efficiency and spectral sensitivity are not required for this part of the work.

Because the CE angle is a function of $1/\beta$,[3] which is slowly varying at high energies, the CE angular distribution of high-energy beams is largely determined by the angular distribution of the charged particles and not by their energies. Due to scattering, in Fig. 10 we therefore observe a strong variation in the simulated electron beam CE angular distribution with beam quality and depth, with a narrower distribution at high beam qualities and shallow depths peaked at the 42° CE angle of relativistic electrons in water[3,14] and a shift of the peak towards higher θ with increasing depths in 10(b). In comparing Fig. 10(c) with a corresponding 6 MV photon beam study,[10] we see that, as expected, due to transient charged particle equilibrium, the photon beam CE angular distribution is much less depth dependent. Note that 90° detection may not be optimal in terms of signal intensity. As we have shown in this study, however, CE by high-energy electron beams is readily detectable at 90°, even at superficial depths. Although this appears not to be the case in Fig. 10(a), this is an effect of normalization. In fact, the distribution with the lowest normalized value at 90° (20 MeV, 1 mm) corresponds to 50% of the absolute CE power of the distribution with the highest normalized value (6 MeV, R_{50}). At all depths and energies shown, the CE power at 90°, integrated over a 400–600 nm optical bandwidth, within an optical AA of ±5°, in a 1 cm^3 volume of water, and at a dose rate of 400 MU/min is of the order of 1–10 pW.

It is also evident in Fig. 10 that 90° detection is less sensitive to angle variations than detection near 42° and, in Fig. 11, we further show that the simulated PDC at 90° ± 5° is relatively insensitive to ±4° variation in $\delta\theta$. The 0.5-mm upstream shift with a $\delta\theta$ increase from 1° to 9° is due to an increasing contribution from electrons of higher energies, which are more forward directed [see Eq. (4)]. The locally normalized absolute CE (per mass) variation for ±0.1° variations about the $\theta \pm \delta\theta = 90° \pm 5°$ configuration was found to be within ±2.2% at all depths and beam energies. This corresponds to a relative standard uncertainty component (rectangular distribution) of <1.3% (k = 1). This was also confirmed experimentally in Fig. 12, where a ±10% variation in the mass-normalized optical readings was observed on average per ±0.5° variation in the optics AA. However, manufacturers (e.g., Edmund Optics Ltd, Barrington, NJ, USA)[32] cite achievable angle tolerances of the order of arcseconds (<0.01°), which would bring the corresponding uncertainty down to <0.1%. Furthermore, for relative CE-based dosimetry, the relevant uncertainty is that of the PDC, which was found to be <0.1% for $\delta\theta$ variations of 0.1°.

In Fig. 13, we further demonstrate ≤1% (k = 1) uncertainty contribution of the robustness of our provisional detector design (Fig. 1) for PDC >50% to reassembly, refocusing, collimation, lens material composition, and ±1-cm changes in the focusing lens position and focal length (i.e., ± 0.5 cm changes in the convex radius of curvature of the right lens in Fig. 1). The switch from a 2- to 5-cm focal length plano-convex focusing lens (f/2) and insertion of an aperture between the fiber and focusing lens to limit the 2° AA in Fig. 13 is expected to reduce optical aberrations due to the decreased curvature of the 5-cm lens and restriction of the marginal acceptance by the aperture.[27] The agreement between the 2° curves in Fig. 13, however, indicates that the effectiveness of these changes in reducing the aberrations is minor with this setup. The aberrations are expected to be minimized with detection optics optimization through modeling using diffraction-limited optics. An effort was made in this study to minimize the aberrations by use of two plano-convex lenses oriented as in Fig. 2 and apertures on both sides of the lens assembly (see Section 3.B). In addition, the lack of observable volume averaging differences with the two apertures (12 vs 6 mm) at 0° in Fig. 13 may be due to weighting of the optics acceptance towards the optical axis or to changes in the aberrations as a result of stopping down. On the other hand, volume averaging is evident in comparing the PDC curves with 0° vs 2° AA.

Background contributions to the measurements from points outside the (ray optics-approximated) sensitive volume in the water were also evaluated in Section 4.D.5. The background signal was found to be mainly due to couch scatter entering the optics (fiber/lenses) and generating CE within the optics themselves. This is because the background signal was (a) characteristic of photon scatter, (b) strongly dependent on the longitudinal couch position for the same numerical aperture, and (c) independent of the longitudinal position of the optics for the same couch position and numerical aperture. In addition, CE contributions from the water tank wall near the detector (see Fig. 1) were negligible, while contributions from the far-field wall constituted up to $\sim 5\%$ of the local background-subtracted signal and were due to reflections. Therefore, while the background signal (generated in the fiber and optics) with this setup can be acquired by closing the detector end aperture, we recommend blacking out the far wall. Finally, background contributions from points outside the ray optics-approximated sensitive volume, due to optical aberrations, were shown to increase by up to 2% of the maximum CE reading per 1-cm increase in the radius of curvature of the curved (nonplano) side of the collimating lens (i.e., the left lens in Fig. 1).

In place of the 2D imaging systems used in the literature to detect CE in water,[6,10,11] we use a pair of plano-convex lenses with apertures focused on beam axis and feeding into a single long multimode fiber optic cable, leading to a spectrometer outside the treatment room (see Fig. 1). This is motivated by the fact that it is a simple detector, individual optical components can be readily modified and reassembled, and more importantly it can be easily modeled and allows for a more direct comparison between MC and experiment. There is no image distortion, vignetting,[6] or varying acceptance angles with depth.[10] With the exception of superficial measurements, the sensitive volume is constant with depth within the experimental uncertainties. In addition, the use of a spectrometer provides spectral measurements (Section 4.D.1) and its positioning outside of the treatment room eliminates scatter radiation noise.[6] This setup can be extended to 2D by use of lens and fiber arrays in combination with a multichannel spectrometer.

A limitation of our detector design is the use of spherical lenses, which nevertheless made possible the evaluation of the effect of optical aberrations (Sections 4.D.4 and 4.D.5). In addition, the response spanned the entire water tank (Fig. 1) and our results are relative. As discussed throughout, this work aims to motivate optical design and characterization of a CE-based dosimeter with narrow response on beam axis, which requires further investigation and may potentially involve optical sectioning techniques[5] or 4π detection (via, e.g., tomographic reconstruction combining projections from nonparallel sets of planes). CE detector optical design, absolute irradiance calibration, and characterization will allow evaluation of detector-related uncertainties specific to CE-based dosimetry and comparison with current practice in reference and relative dosimetry. CE may be especially promising for small-field dosimetry[33] due to the small resolutions achievable via, for example, optical sectioning.[5]

A limitation of the formalism outlined in Section 2 is the beam quality and depth dependence of the CE-to-dose conversion. We take an in-depth look at the corresponding uncertainty contributions to CE-based electron beam dosimetry in Paper II.[12] For photon beams, weaker overall dependencies are expected as discussed throughout this work and observed in the literature.[7,10,11] These limitations pave important venues to be explored in the future efforts toward full clinical implementation of CE-based dosimetry.

6. CONCLUSIONS

Cherenkov emission-based dosimetry of both large- and small-field external radiotherapy beams has received much attention over the last decade as it carries promise as an in-water, perturbation-free, high-resolution technique. That is, it involves detection of CE from the beam directly in water with a detector positioned out of the beam at resolutions potentially of the order of micrometers. In this study, we consider a broad-beam, central-axis CE-to-dose conversion formalism, modify the SPRRZnrc Monte Carlo code for calculation of the conversion, and carry out relative experimental validation of the code with a simple detector in electron beams. Photon beams are expected to be less sensitive to experimental uncertainties and this is confirmed by comparison with the literature. Electron beam CE-based dosimetric uncertainties related to the CE-to-dose conversion are addressed in greater detail in a companion study. The aim of the current study is to motivate detector development and characterization of a CE-based dosimeter and phantom system, which is envisioned to employ optical sectioning or tomographic techniques and will make possible evaluation of the detector-related uncertainties specific to CE-based dosimetry in relation to specific applications in current practice. CE may carry promise as a small-field technique due to the small resolutions achievable in optical imaging.

ACKNOWLEDGMENTS

The authors thank Joe Larkin of the McGill University Health Centre for help with the construction of the experimental setup, Francois Therriault-Proulx of Centre Hospitalier Universitaire de Montréal for valuable discussions on optical instrumentation, and Marc-André Renaud for help with setting up the simulations. YZ acknowledges partial support by the CREATE Medical Physics Research Training Network grant of the Natural Sciences and Engineering Research Council (NSERC) (#432290), CREATE Integrated Sensor Systems grant of NSERC (#371305), and Bourses de doctorat en recherche (B2) du Fonds de recherche du Québec — Nature et technologies (FRQNT) (#184385). This work was partially supported by NSERC (#RGPIN-2014-06475, #231909).

CONFLICTS OF INTEREST

The authors have no conflicts to disclose.

[a]Author to whom correspondence should be addressed. Electronic mail: yana.zlateva@mail.mcgill.ca; http://www.mcgill.ca/medphys/.

REFERENCES

1. Cherenkov P. "Vidimoe svechenie chistykh zhidkostei pod deistviem gamma-radiatsii" (Visible glow of pure liquids under gamma radiation). *Dokl Akad Nauk SSSR*. 1934;2:451–457.
2. Tamm I, Frank I. "Kogerentnoe izluchenie bystrogo elektrona v srede" (Coherent radiation of a fast electron in a medium). *Dokl Akad Nauk*. 1937;14:107–112.
3. Jelley JV. Cerenkov radiation and its applications. *Br J Appl Phys*. 1955;6:227–232.
4. Malacara-Hernández D, Malacara-Hernández Z. *Handbook of Optical Design*, 3rd ed. Boca Raton, FL: CRC Press; 2014.
5. Agard DA, Hiraoka Y, Shaw P, Sedat JW. Chapter 13: Fluorescence microscopy in three dimensions. In: Taylor DL, Wang Y-L, eds. *Fluorescence Microscopy of Living Cells in Culture Part B. Quantitative Fluorescence Microscopy-Imaging and Spectroscopy, Volume 30 of Methods in Cell Biology*. Cambridge, MA: Academic Press; 1989: 353–377.
6. Helo Y, Rosenberg I, D'Souza D, et al. Imaging Cerenkov emission as a quality assurance tool in electron radiotherapy. *Phys Med Biol*. 2014;59:1963–1978.
7. Glaser AK, Zhang R, Gladstone DJ, Pogue BW. Optical dosimetry of radiotherapy beams using Cherenkov radiation: the relationship between light emission and dose. *Phys Med Biol*. 2014;59:3789–3811.
8. Almond PR, Biggs PJ, Coursey BM, et al. AAPM's TG-51 protocol for clinical reference dosimetry of high-energy photon and electron beams. *Med Phys*. 1999;26:1847–1870.
9. Kawrakow I. Accurate condensed history Monte Carlo simulation of electron transport. I. EGSnrc, the new EGS4 version. *Med Phys*. 2000;27:485–498.
10. Glaser AK, Davis SC, McClatchy DM, Zhang R, Pogue BW, Gladstone DJ. Projection imaging of photon beams by the Čerenkov effect. *Med Phys*. 2013;40:012101-1–012101-13.
11. Glaser AK, Voigt WHA, Davis SC, Zhang R, Gladstone DJ, Pogue BW. Three-dimensional Cerenkov tomography of energy deposition from ionizing radiation beams. *Opt Lett*. 2013;38:634–636.
12. Zlateva Y, Muir B, Seuntjens J, El Naqa I. Cherenkov emission-based external radiotherapy dosimetry: II. Electron beam quality specification and uncertainties. *Med Phys*. 2019; [Epub ahead of print].
13. Andreo P, Burns D, Hohlfeld K, et al. Absorbed Dose Determination in External Beam Radiotherapy, Technical Report Series 398, International Atomic Energy Agency, Vienna; 2000.
14. Daimon M, Masumura A. Measurement of the refractive index of distilled water from the near-infrared region to the ultraviolet region. *Appl Opt.* 2007;46:3811–3820.
15. Spencer LV, Attix FH. A theory of cavity ionization. *Radiat Res*. 1955;3:239–254.
16. McEwen M, DeWerd L, Ibbott G, et al. Addendum to the AAPM's TG-51 protocol for clinical reference dosimetry of high-energy photon beams. *Med Phys*. 2014;41:041501-1–041501-20.
17. International Commission on Radiation Units and Measurements. Key data for ionizing-radiation dosimetry: measurement standards and applications. Technical Report 90, Journal of the ICRU Volume 14 No 1, Oxford University Press, Oxford, UK; 2014.
18. Rogers DWO, Faddegon BA, Ding GX, Ma C-M, We J, Mackie TR. BEAM: A Monte Carlo code to simulate radiotherapy treatment units. *Med Phys*. 1995;22:503–524.
19. Rogers D, Walters B, Kawrakow I. BEAMnrc Users Manual. Technical Report PIRS-0509(A)revL, National Research Council of Canada, Ottawa, Canada; 2012.
20. Kawrakow I, Mainegra-Hing E, Rogers D, Tessier F, Walters B. The EGSnrc Code System: Monte Carlo Simulation of Electron and Photon Transport. Technical Report PIRS-701, National Research Council of Canada, Ottawa, Canada; 2011.
21. Rodrigues A, Sawkey D, Yin F-F, Wu Q. A Monte Carlo simulation framework for electron beam dose calculations using Varian phase space files for TrueBeam Linacs. *Med Phys*. 2015;42:2389–2403.
22. Zlateva Y. GitHub repository, scrrznrc. Commit, https://github.com/yanazlateva/scrrznrc/tree/f5356f63166a538ebd3b8f84775b5de69e895428, 2019.
23. Rogers D, Kawrakow I, Seuntjens J, Walters B, Mainegra-Hing E. NRC User Codes for EGSnrc. Technical Report PIRS-702(RevB), National Research Council of Canada, Ottawa, Canada; 2003.
24. Hale GM, Querry MR, Optical constants of water in the 200-nm to 200-μm wavelength region. *Appl Opt*. 1973;12:555–563.
25. Glaser AK, Davis SC, Voigt WHA, Zhang R, Pogue BW, Gladstone DJ. Projection imaging of photon beams using Čerenkov-excited fluorescence. *Phys Med Biol*. 2013;58:601–619.
26. Jean E, Delage M-E, Beaulieu L. Investigation of the quinine sulfate dihydrate spectral properties and its effects on Cherenkov dosimetry. arXiv preprint arXiv:1809.02048; 2018.
27. Smith W. The Primary Aberrations, In: *Modern Optical Engineering*, 4th ed. McGraw Hill professional, chapter 5. New York City, NY: McGraw-Hill Education; 2007.
28. Das IJ, Cheng C-W, Watts RJ, et al. Accelerator beam data commissioning equipment and procedures: Report of the TG-106 of the Therapy Physics Committee of the AAPM. *Med Phys*. 2008;35: 4186–4215.
29. Glaser A, Andreozzi J, Zhang R, Pogue BW, Gladstone DJ. Optical cone beam tomography of Cherenkov-mediated signals for fast 3D dosimetry of X-ray photon beams in water. *Med Phys*. 2015;42:4127–4136.
30. Bruza P, Andreozzi JM, Gladstone DJ, Jarvis LA, Rottmann J, Pogue BW. Online combination of EPID & Cherenkov imaging for 3-D dosimetry in a liquid phantom. *IEEE Trans Med Imaging*. 2017;36:2099–2103.
31. Agostinelli S, Allison J, Amako K, et al. Geant4-a simulation toolkit. *Nucl Instrum Methods Phys Res Sect A*. 2003;506:250–303.
32. Edmund Optics Inc. Understanding Optical Specifications. https://www.edmundoptics.com/resources/application-notes/optics/understanding-optical-specifications/; 2018. Accessed on 2018-10-20.
33. Crop F, Reynaert N, Pittomvils G, et al. The influence of small field sizes, penumbra, spot size and measurement depth on perturbation factors for microionization chambers. *Phys Med Biol*. 2009;54:2951–2969.